JOURNAL OF MATERIALS SCIENCE **37** (2002) 5209–5214

Microstructure and strength of a deformation processed Al-20%Sn *in situ* composite

K. XU*, K. WONGPREEDEE, A. M. RUSSELL
Ames Laboratory of the U.S. Department of Energy and Materials Science and Engineering Department, Iowa State University, Ames, IA 50011, USA
E-mail: xukai@iastate.edu

An Al-20 vol% Sn metal-metal composite was deformation processed by extrusion, swaging, and wire drawing to a total true strain of 7.4, resulting in a microstructure with Sn filaments in an Al matrix. Both the size and spacing of the Sn filaments decreased as deformation processing progressed. The strength of these composites increased exponentially with the reduction in spacing of the Sn filaments. Immediately after deformation, the Sn second phase showed a convoluted, ribbon-shaped filamentary morphology, but the Sn filaments spheroidized during prolonged storage at room temperature. A thermodynamic assessment is presented for this spheroidization phenomenon.

1. Introduction

If the flow stresses of two metal phases are similar, severe mechanical deformation of a two-phase microstructure of these metals will co-deform the two phases in roughly equal amounts. These Deformation-processed Metal Metal Composites (DMMCs) possess extraordinary mechanical and electrical properties. Since the filamentary microstructure is formed within the composites during deformation, these composites are sometimes called *in situ* composites.

The typical method of making DMMCs is to prepare starting billets by ingot casting or by powder metallurgy followed by rolling or by axisymmetric deformation such as extrusion, swaging, and wire drawing. Extensive deformation will produce a composite material with elongated filaments aligned parallel to the deformation direction.

Most of the initial studies on DMMCs were conducted on composites with a face centered cubic (fcc) matrix containing about 20 volume percent of a body centered cubic (bcc) secondary reinforcing phase. Cu-X (where X is a bcc metal such as Nb, Ta, Cr, W or Fe) systems [1–9] were the most thoroughly studied. Bevk, Harbison, and Bell [1] first reported a Cu-Nb DMMC in the 1970s that was intended to serve as a precursor material for production of superconducting wire. A Cu-18 vol%Nb DMMC was made with an ultimate tensile strength of 2200 MPa at a deformation true strain of 11.5. This strength level was as high as the best Cu whisker strengths. A deformation true strain parameter, $\eta = \ln(A_i/A_f)$, was used to characterize the degree of deformation, where A_i and A_f are the specimen's initial and final transverse areas respectively. In Cu-X DMMCs, the bcc second phase developed a $\langle 110 \rangle$ fiber texture that limits the deformation of the second phase to plane strain [1, 10]. As a result, the typical microstructure of fcc/bcc DMMCs is a convoluted, ribbon-shaped second phase embedded in the matrix.

In addition to Cu-X DMMCs, other DMMCs with hexagonal close packed (hcp) metals were reported in the 1990s. Experiments in the Ti-Y system have examined Ti matrix DMMCs containing 20% Y and 50% Y. Ti-Y was first hot deformed followed by cold deformation with intermediate annealing at 890 K. A deformation true strain of 7.3 was achieved with this procedure, and an ultimate tensile strength of 950 MPa was reported by Russell *et al.* [11, 12]. The Y filaments had a kinked ribbon-shaped morphology similar to that of the Nb filaments in the Cu-Nb DMMCs. Both Ti and Y adopted a pronounced $\langle 10\bar{1}0 \rangle$ fiber texture along the wire axis, which limited slip to plane strain just as had been observed with the $\langle 110 \rangle$ texture in the bcc phases of the Cu-X DMMCs. Other DMMCs containing hcp metals have since been reported, including Mg-Ti [13, 14], Al-Ti [15], and Al-Mg [16]. All hcp second phases showed the same ribbon shaped filamentary microstructure due to $\langle 10\bar{1}0 \rangle$ fiber texture of second phases.

With the exception of early studies on pearlitic steel [17], all the DMMCs that have been investigated have used metals with fcc, bcc, and/or hcp crystal structures. In this study, an fcc Al matrix DMMC containing body centered tetragonal (bct) Sn as the second phase was produced. Although the material displayed the familiar continuous elongated filamentary microstructure in the wire direction immediately after deformation, the microstructure spheroidized during prolonged storage at room temperature.

*Author to whom all the correspondence should be addressed.

2. Experimental procedure

High purity Al powder (99.99% purity) with a particle size of 45–75 μm was produced by the gas atomization method at Ames Laboratory. Sn powder (99.80% purity) with a particle size smaller than 45 μm (-325 mesh) was mixed with this Al powder in a ratio of 80 vol% Al to 20 vol% Sn, which is hereinafter referred to as Al-20Sn. The powders were cold isostatically pressed at 130 MPa after blending. The 37 mm diameter green compact was put into a Cu can with an outside diameter of 50.8 mm. The Cu can and compact were soldered shut and evacuated followed by extrusion at room temperature through a 25.4 mm diameter die. After extrusion, the sample was water quenched immediately to remove the heat generated by the extrusion.

The extruded Al-20Sn rod with Cu sleeve was swaged at room temperature to a deformation true strain of $\eta = 3.20$ to a diameter of 7.62 mm. The Cu sleeve was removed by machining at this point. The bare Al-20Sn was swaged to a diameter of 3.0 mm ($\eta = 4.40$). Finally, the sample was wire drawn to a diameter of 0.48 mm ($\eta = 7.41$). The deformation was terminated at $\eta = 7.41$ due to the small size of the wire. Metallography coupons and two tensile specimens were cut from the material at each of the deformation true strains $\eta = 3.20$, 4.40, 5.54, 6.05, and 7.41.

Tensile tests were performed for all specimens with $\eta < 6$ following ASTM standard E8 [18]. For smaller diameter wires with $\eta > 6$, tensile specimens were made by embedding the two wire ends into two small Cu sleeves with adhesive followed by deforming the Cu sleeves around the specimen ends to form grips for tensile testing. All tensile tests were done at room temperature with a strain rate of 1.0 mm/min (for $\eta < 6$), and 0.15 mm/min (for $n > 6$).

An Amray 1845 field emission gun scanning electron microscope (SEM) was used to observe the Al-20Sn DMMC microstructure.

3. Results

3.1. Microstructure characterization

Figs 1–3 show the microstructures of Al-20Sn DMMCs at different deformation true strains. As shown in Fig. 1, the Sn phase displayed a convoluted ribbon shape in transverse section, which may have resulted from plane strain of the bct Sn. In the longitudinal section, the Sn phase was present as long filaments at low deformation true strain (Fig. 2). With increasing η, the Sn filaments gradually evolved into partially spheroidized particles as shown in Fig. 3 rather than the long, continuous filaments normally seen in other DMMCs.

This spheroidization of the filaments in the longitudinal direction has been observed in other DMMCs after exposure to elevated temperature, but has heretofore not been reported at room temperature. The spheroidization seen here may be caused by the low melting point of Sn (505 K) and the shape irregularities of filaments that normally occurs along the longitudinal direction after deformation processing. During extrusion, the specimen briefly experienced a temperature at or slightly above 370 K due to the severe mechanical deformation. The specimen temperature was also raised briefly ($\sim$50 K above ambient) in subsequent swaging and wire drawing operations. In addition, a time period of 1.5 to 2.4 months elapsed between successive deformation procedures and between deformation and preparation of the metallography specimens shown in Figs 2 and 3. During the time periods that the specimens were stored at room temperature, they were at nearly 60% of the homologous melting temperature of Sn.

Kampe and Courtney [19, 20] studied the high temperature behavior of DMMCs, and reported that capillary force and chemical potential gradients drove atomic motion that eventually led to spherical particles.

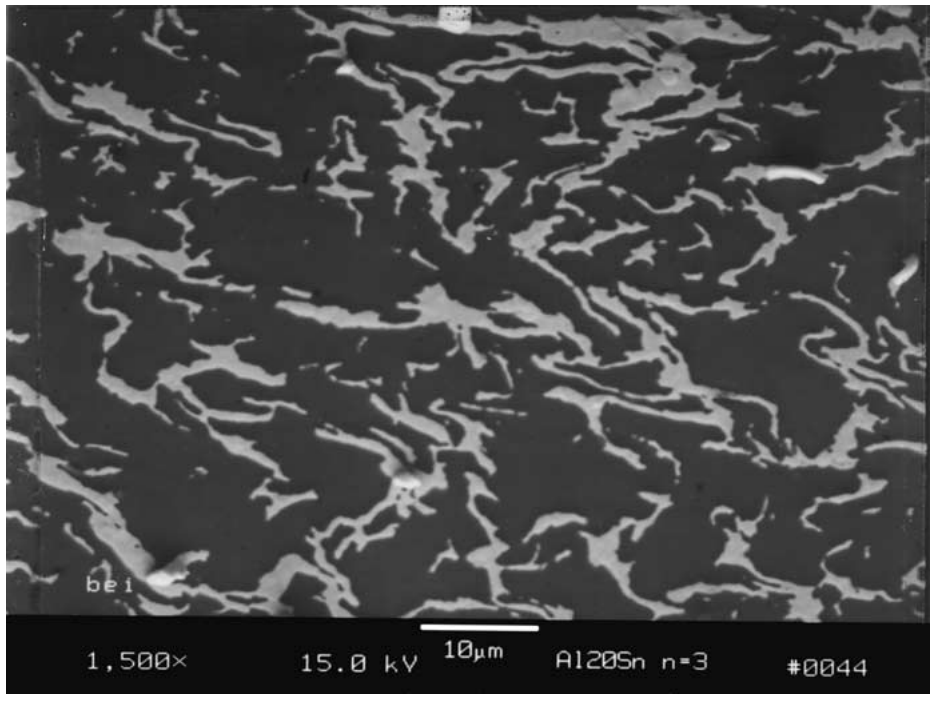

Figure 1 Transverse section SEM micrograph of Al-20Sn ($\eta = 3.20$). The Al matrix is dark gray, and the Sn filaments are light gray.

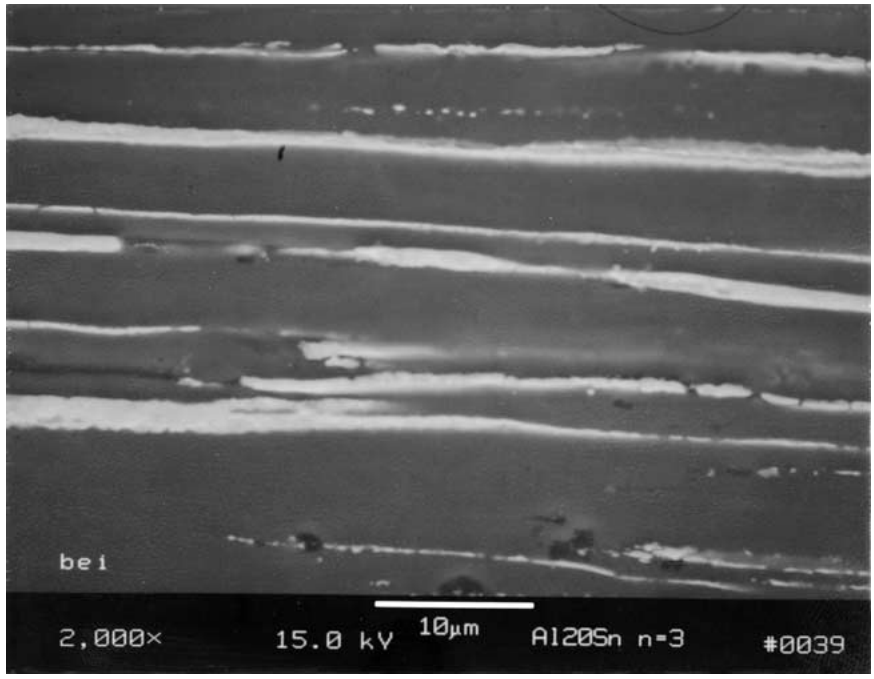

Figure 2 Longitudinal section SEM micrograph of Al-20Sn ($\eta = 3.20$) photographed shortly after deformation. The Al matrix is dark gray, and the Sn filaments are light gray.

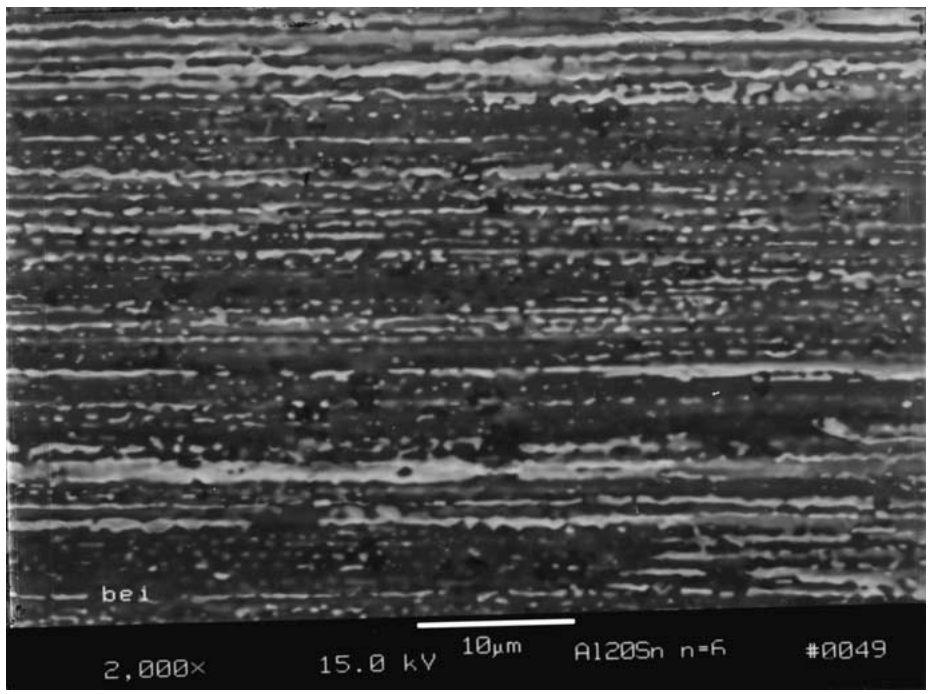

Figure 3 Longitudinal section SEM micrograph of Al-20Sn ($\eta = 6.05$) after storage for several Ms at room temperature. Note the spheroidization of the Sn filaments in comparison to their shape in Fig. 2. The Al matrix is dark gray, and the Sn filaments are light gray.

3.2. Mechanical properties of Al-Sn composite wire

The effects of deformation true strain on ultimate tensile strength (UTS) of Al-20Sn are shown in Fig. 4. Similar to the mechanical behavior of other DMMCs, the tensile strength of Al-20Sn composite increased substantially with deformation true strain. This finding is inconsistent with a simple rule of mixtures model for composite strength, since the strength of this Al-20Sn composite is much higher than the strength of either Sn or high purity Al, and neither of these metals work hardens sufficiently to account for this strengthening effect.

4. Discussion

4.1. Explanation for spheroidization

As shown in Section 3, spheroidization occurred in the longitudinal direction for Al-20Sn DMMCs after prolonged storage at room temperature. We believe the presence of longitudinal perturbations in the cylinder radius of the Sn filaments caused the conversion of

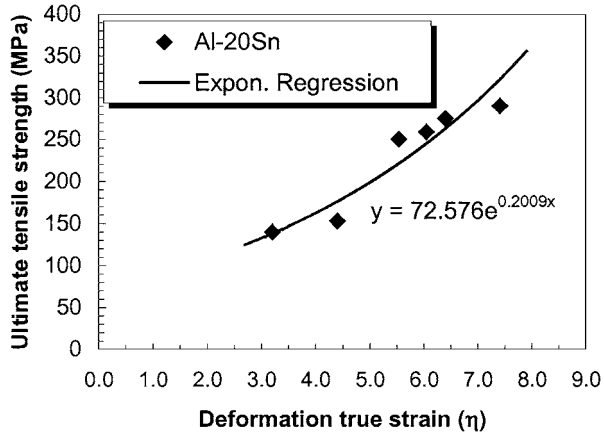

Figure 4 The dependence of UTS on deformation true strain for Al-20Sn.

roughly cylindrical filaments into spheres. DMMCs typically have an abundance of surface and size irregularities along the longitudinal direction of the second phase filaments. For a cylindrical filament with a longitudinal perturbation in radius, there are two principal radii of curvature as shown in Fig. 5. R_1 is the primary radius of the cylinder, and R_2 is the secondary radius. From location A to location B, the increase in R_1 induces transport of filament material from A to B, which tends to increase the magnitude of the initial perturbation. In opposition to this trend, the increase in R_2 from location A to location B transports filament material from B to A, opposing growth of the perturbation. If a critical wavelength λ_{crit} is reached, there is an equilibrium between A and B with no net material flow between A and B. If the equilibrium is not maintained, atoms move from A to B, the perturbation will become more pronounced, and spheroidization of the filaments will eventually occur. This fluctuation in cylindrical filament radius, combined with the high homologous temperature at which these specimens were stored, is believed to be the cause of the extensively spheroidized microstructure shown in Fig. 3.

Chemical potential difference is believed to be the driving force for spheroidization of the Sn phase. To examine the critical condition of a Sn cylinder to predict whether it would remain stable or spheroidize, one could assume that the cylinder has a simple sinusoidal fluctuation as shown in Fig. 5. The profile of the perturbed cylinder is given by $y = R + \delta \sin(2\pi x/\lambda)$, where R is the radius of the cylinder, λ is the wavelength of perturbation, x is the distance along the cylinder length, and δ is the amplitude of the perturbation. If the value of δ is assumed to be infinitesimal, only linear terms of δ are significant and higher order terms of δ (i.e., δ^2, δ^3) are negligible. Since the cross section of this perturbed cylinder remains circular, both principal curvatures have to be considered at each point of the cylinder.

According to the Gibbs-Thompson equation, the chemical potential of an atom on a curved surface can be expressed as $\mu = \mu_0 + \gamma V \kappa$, where μ_0 is the chemical potential of an atom at a flat surface, γ is surface energy, κ is surface curvature, and V is atomic volume. For a function $y = f(x)$, curvature

$$\kappa = \frac{|y''|}{(1 + y'^2)^{3/2}}$$

where y' is the first derivative and y'' is the second derivative of function y.

For a curved surface, the total curvature at one point can be calculated as:

$$\kappa_T = \kappa_1 + \kappa_2$$

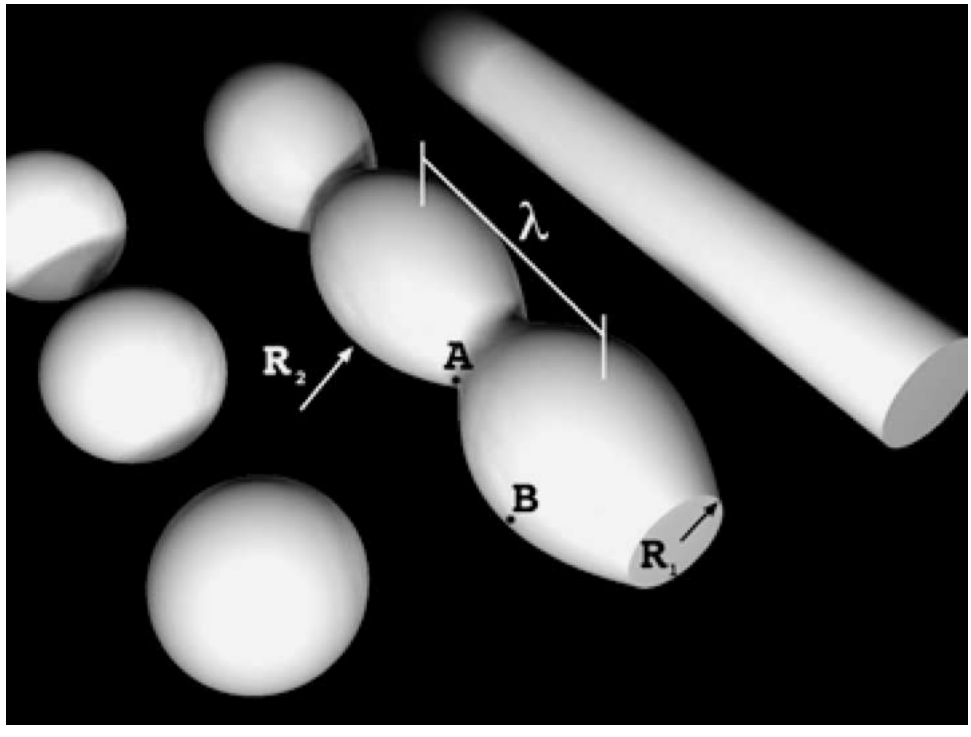

Figure 5 A idealized illustration of conversion from a cylindrical filament into spheres.

Therefore, curvature at point A and B can be derived as:

$$\kappa_A = -\frac{4\pi^2\delta}{\lambda^2} + \frac{1}{R-\delta}$$

$$\kappa_B = -\frac{4\pi^2\delta}{\lambda^2} + \frac{1}{R+\delta}$$

The chemical potential at point A and B can be derived from the Gibbs-Thompson equation as:

$$\mu_{\mathrm{A}} = \mu_0 + \gamma V\left(-\frac{4\pi^2\delta}{\lambda^2} + \frac{1}{R-\delta}\right)$$

$$\mu_{\mathrm{B}} = \mu_0 + \gamma V\left(\frac{4\pi^2\delta}{\lambda^2} + \frac{1}{R+\delta}\right)$$

If $\mu_{\mathrm{A}} = \mu_{\mathrm{B}}$, then a critical distance λ_{crit} can be determined to be $\lambda_{\mathrm{crit}} = 2\pi R$. When the wavelength of a cylindrical filament is at this critical distance, the chemical potential at point A is exactly equal to that at point B, and these expressions predict no atomic motion between points A and B.

If $\mu_{\mathrm{A}} > \mu_{\mathrm{B}}$, it can be determined that $\lambda > 2\pi R$. In this case the chemical potential at point B is lower than that at point A, atoms will move from point A to point B; this net migration of atoms renders the cylindrical geometry unstable and leads eventually to spheroidization.

If $\mu_{\mathrm{A}} < \mu_{\mathrm{B}}$, it can be determined that $\lambda < 2\pi R$. Since the chemical potential at point A is lower than that at point B, atoms will move from point B to point A, which promotes the stability of the cylinder and prevents spheroidization of the cylinder.

4.2. Strengthening of Al-20Sn composite

As noted in Section 3, the rule of mixtures approach fails to account for the strength of the Al-20Sn DMMC. Many studies have been done to correlate UTS with deformation true strain for DMMCs; an exponential relationship has frequently been observed to exist between ultimate tensile strength and deformation true strain [21, 22]. The Hall-Petch barrier model is often used to explain the strengthening mechanism of DMMCs. The Hall-Petch model predicts increasing strength as the thickness and spacing of the second phase filaments decrease. With the progressively finer filamentary microstructure that accompanies increasing η, the Sn second phase acts as a more effective network of barriers to dislocation production and movement in the Al phase. Further motion requires generation of new dislocations in the neighboring area by the local stress field produced by the blocked dislocations. As a result, the composite is strengthened.

The Hall-Petch relationship can be applied to DMMCs as:

$$\sigma = \sigma_0 + k\lambda^{-1/2}$$

where σ is the UTS, σ_0 and k are constants, and λ is the filament spacing. Embury has proposed a modified Hall-Petch model to explain the strengthening of DMMCs [21]:

$$\sigma = \sigma_0 + kd_0^{-1/2}\exp(0.25\eta)$$

where σ is UTS, σ_0 and k are constants, d_0 is the initial filament spacing, and η is deformation true strain. This empirical equation was confirmed by Russell *et al*. for a Ti-Y DMMC [11]. Similarly, Sakai *et al*. found that UTS = 565 exp(nη) for a Cu-Ag DMMC where n is a factor that varies with Ag content [22]. By exponential regression, it was found the relationship between UTS and η that best fits the data for Al-20Sn DMMC is:

$$\mathrm{UTS} = 72.6\exp(0.20\eta)$$

5. Conclusions

1. Al-20Sn composite can be deformation processed to a deformation true strain of 7.41. The Sn second phase adopts a convoluted, ribbon shaped filamentary morphology after axisymmetric deformation, which may be due to texture effects in the Sn that restrict its plastic flow to plane strain.

2. The Sn second phase partially spheroidizes during deformation along the longitudinal direction of the wire. This is thought to be due to the low melting temperature of Sn and irregularities in the initial shape of the Sn filaments.

3. A chemical potential gradient is proposed as the driving force for spheroidization. A critical wavelength of $\lambda_{\mathrm{crit}} = 2\pi R$ can be used to determine the spheroidization tendency of a Sn cylinder. When $\lambda > 2\pi R$, spheroidization is predicted to occur.

4. The ultimate tensile strength of Al-20Sn composite increases exponentially with deformation true strain. The relationship between UTS and deformation true strain is $\mathrm{UTS} = 72.6\exp(0.20\eta)$.

Acknowledgements

This work was performed at Ames Laboratory, operated for the US Department of Energy by Iowa State University under contract no. W-7405-Eng-82. The authors thank I. Anderson for providing the GARS Al powder used in this study and L. Lincoln, L. Jones, and P. Wheelock of the Ames Laboratory Materials Preparation Center for preparing the materials used in this study. The authors also are grateful to F. Laabs for his SEM work. Special thanks go to Prof. R. Trivedi for valuable discussions.

References

1. J. BEVK, J. P. HARBISON and J. L. BELL, *J. Appl. Physics* **49** (1978) 6031.
2. W. A. SPITZIG, A. R. PELTON and F. C. LAABS, *Acta Metall.* **35** (1987) 2427.
3. W. A. SPITZIG, C. L. TRYBUS and F. C. LAABS, *Mat. Sci. Eng.* A **145** (1991) 179.
4. S. POURRAHIMI, H. NAYEB-HASHEMI and S. FONER, *J. Mater. Sci. Lett.* **9** (1990) 1484.
5. *Idem.*, *Metall. Trans.* A **23A** (1992) 573.
6. J. D. VERHOEVEN, L. S. CHUMBLEY, F. C. LAABS and W. A. SPITZIG, *Acta Metall.* **39** (1991) 2825.

7. J. D. VERHOEVEN, F. A. SCHMIDT, E. D. GIBSON and W. A. SPITZIG, *J. Metals* **38** (1986) 20.
8. P. D. FUNKENBUSCH, T. H. COURTNEY and D. G. KUBISCH, *Scripta Metall.* **18** (1984) 1099.
9. Y. LENG, T. H. COURTNEY and J. C. MALZAHN KAMPE, *Mat. Sci. Eng.* **94** (1987) 209.
10. W. A. BACKOFEN, "Deformation Processing" (Addison-Wesley, Reading, MA, 1972) p. 51, 75 and 295.
11. A. M. RUSSELL, L. S. CHUMBLEY, T. W. ELLIS, F. C. LAABS, B. NORRIS and G. E. DONIZETTI, *J. Mater. Sci.* **30** (1995) 4249.
12. A. M. RUSSELL, T. W. ELLIS and L. S. CHUMBLEY, *ibid.* **30** (1995) 2070.
13. J. A. JENSEN, A. M. RUSSELL, T. W. ELLIS and L. S. CHUMBLEY, in "Light Metals," edited by J. Evans (TMS, Warrendale, PA (1995) p. 1367.
14. J. A. JENSEN and L. S. CHUMBLEY, *Metallurgical and Materials Transactions* A **29A** (1998) 863.
15. A. M. RUSSELL, T. LUND, L. S. CHUMBLEY, F. C. LAABS, L. L. KEEHNER and J. L. HARRINGA, *Composites: Part A* **30** (1999) 239.
16. K. XU, A. M. RUSSELL, L. S. CHUMBLEY, F. C. LAABS, V. B. GANTOVNIK and Y. TIAN, *J. Mater. Sci.* **34**(24) (1999).
17. J. D. EMBURY and R. M. FISHER, *Acta Metall.* **14** (1966) 147.
18. B. W. CHRIST, *ASM Metals Handbook* **8** (1985) 28.
19. J. C. MALZAHN KAMPE, T. H. COURTNEY and Y. LENG, *Acta Metall.* **37**(7) (1989) 1735.
20. T. H. COURTNEY and J. C. MALZAHN KAMPE, *ibid.* **37**(7) (1989) 1747.
21. J. D. EMBURY, *Scripta Metall.* **27** (1992) 981.
22. Y. SAKAI and H. J. SCHNEIDER-MUNTAU, *Acta Mater.* **45**(3) (1997) 1017.

Received 26 February
and accepted 15 March 2002